

Modeling and Control of a Novel Variable Stiffness Three DoFs Wrist

Giuseppe Milazzo¹, Manuel Giuseppe Catalano¹, Antonio Bicchi^{1,2}, and Giorgio Grioli^{1,2}

Abstract

This study introduces an innovative design for a Variable Stiffness 3 Degrees of Freedom actuated wrist capable of actively and continuously adjusting its overall stiffness by modulating the active length of non-linear elastic elements. This modulation is akin to human muscular cocontraction and is achieved using only four motors. The mechanical configuration employed results in a compact and lightweight device with anthropomorphic characteristics, making it potentially suitable for applications such as prosthetics and humanoid robotics. This design aims to enhance performance in dynamic tasks, improve task adaptability, and ensure safety during interactions with both people and objects.

The paper details the first hardware implementation of the proposed design, providing insights into the theoretical model, mechanical and electronic components, as well as the control architecture. System performance is assessed using a motion capture system. The results demonstrate that the prototype offers a broad range of motion ($[55, -45]^\circ$ for flexion/extension, $\pm 48^\circ$ for radial/ulnar deviation, and $\pm 180^\circ$ for pronation/supination) while having the capability to triple its stiffness. Furthermore, following proper calibration, the wrist posture can be reconstructed through multivariate linear regression using rotational encoders and the forward kinematic model. This reconstruction achieves an average Root Mean Square Error of 6.6° , with an R^2 value of 0.93.

Keywords

Variable Stiffness, Articulated Soft Robots, Parallel Manipulator, Wrist, Prosthesis.

1 Introduction

One of the challenges of modern robotics is to craft machines that can physically interact and cooperate with people. Taking inspiration from humans, compliant end-effectors have proven their capability to adapt using simple actuation and control systems in various applications, ranging from industrial [Firth et al. \(2022\)](#), [Zongxing et al. \(2020\)](#), to prosthetics [Tavakoli and de Almeida \(2014\)](#) and service robotics [Tröbinger et al. \(2021\)](#). However, to promote the simplicity of the hardware, robotic limbs usually equip rigid and underactuated serial wrist joints [Bajaj et al. \(2019\)](#), [Fan et al. \(2022\)](#). Nonetheless, wrist articulation plays a crucial role in manipulation tasks since it allows for varying the hand pose to reach the best posture for grasping an object. Therefore, a complete wrist joint should have 3 DoFs to freely orient the end-effector in a tridimensional space.

Many studies prove that human beings adjust the stiffness of their limbs by exploiting muscular cocontraction to adapt to tasks of different natures. In summary, a large stiffness performs better in resisting perturbations and accomplishing precision tasks, while a soft behavior is more suitable for those assignments that require exploring an unknown environment with small interaction forces [Blank et al. \(2014\)](#), [Borzelli et al. \(2018\)](#), [Osu et al. \(2004\)](#). Therefore, it is desirable to replicate this feature of controllable impedance also in robots. One possible way is to adjust the stiffness of rigid manipulators via software, taking advantage of established impedance control techniques [Hogan \(1985\)](#), [Yellewa et al. \(2022\)](#).

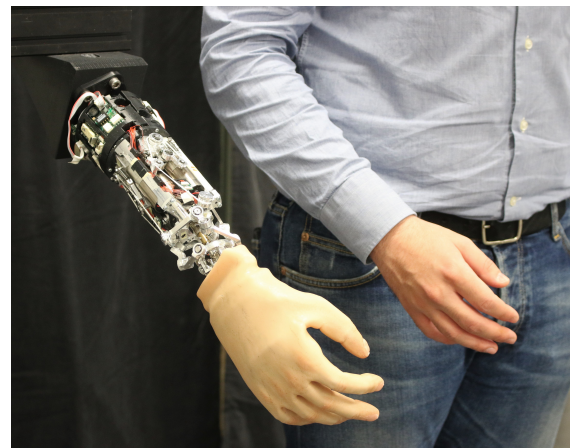


Figure 1. The VS-Wrist compared to a human forearm (model's size: forearm length 247 mm, forearm circumference 265 mm. Comprised between the 5th and 50th percentile male [NASA \(1995\)](#)).

¹Soft Robotics for Human Cooperation and Rehabilitation, Istituto Italiano di Tecnologia, Genova, Italy

²Centro di Ricerca Enrico Piaggio, Università di Pisa, Pisa, Italy.

Corresponding author:

Giuseppe Milazzo, Soft Robotics for Human Cooperation and Rehabilitation, Istituto Italiano di Tecnologia, Via S. Quirico, 19d, 16163, Genova, Italy.

Email: giuseppe.milazzo@iit.it

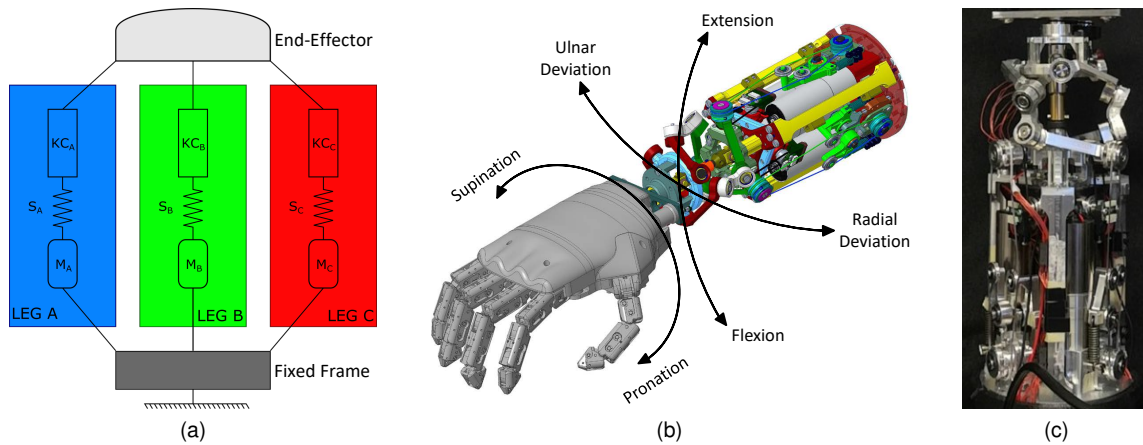


Figure 2. Panel (a) depicts a schematic architecture of the 2 DoFs VS joint integrated into the VS-Wrist. Its kinematic configuration is a parallel manipulator that achieves hemispherical movements of the coupler. Each leg, distinguished by a specific color, consists of a motor unit, a non-linear elastic transmission, and a kinematic chain of four revolute joints. Panel (b) displays the CAD of the VS-Wrist equipping a robotic prosthetic hand and highlights its DoFs. Panel (c) shows a close-up picture of the prototype.

Another possibility involves employing soft robots that embed Variable Stiffness (VS) in their hardware implementation. In contrast to classical machines, soft robots are better suited for applications involving interactions with the environment, prioritizing safety and robustness over the power and precision requirements typical of industrial manipulators. Articulated soft robots achieve this goal by embedding compliant elements in their actuation or transmission, resulting in a behavior comparable to the musculoskeletal system of vertebrates [Migliore et al. \(2005\)](#). In addition, using redundant non-backdrivable actuators, the elastic elements can apply constant forces to increase the stiffness of the joint without requiring a continuous input of energy.

Passive stiffness regulation offers several advantages when compared to impedance control. Active systems use joint movement and interaction forces measurements to modulate feedback gains, changing the effective joint stiffness. However, actively controlling impedance in torque-controlled robots and backdrivable variable stiffness joints requires either high computational cost or a constant energy drain. These drawbacks are particularly relevant to mobile robots and prostheses, where the entire device must match restrictive size and weight constraints that limit the computational power and battery capacity [English and Russell \(1999\)](#). Moreover, [Haddadin et al. \(2007\)](#) shows that, concerning safety, even if impacts are detected timely, the motors could not react quickly enough with solely an impedance control. Therefore, the system should be considered stiff during impacts, making impedance-controlled robots potentially dangerous. In contrast, compliant mechanisms protect the device during external impacts by decoupling the output link from the rest of the system. Furthermore, soft robots are more robust since they can remain compliant even when the actuators are disabled or faulty [Albu-Schaffer et al. \(2008\)](#). Additionally, the energy stored in the elastic elements could reduce power consumption and enhance motor abilities in explosive movements and cyclic tasks [Albu-Schaffer et al. \(2008\)](#), [Haddadin et al. \(2011\)](#), [Grioli et al. \(2015\)](#).

Despite the numerous advantages of VS actuation, artificial wrists commonly lack this feature. Some commercial passive wrists¹ embed elastic elements to comply along flexion/extension movements [Archer et al. \(2011\)](#). Yang et al. present a serial 2 DoFs soft wrist made of the sequence of two continuum bending and torsion modules, which can vary the stiffness of the bending joint by inflating a balloon [Yang et al. \(2022\)](#). Von Drigalski et al. show a passive 6 DoFs wrist for industrial applications with inherent compliance that can switch to the rigid configuration using an external actuator [von Drigalski et al. \(2020\)](#). Recently, researchers employed powered one DoF VS joints for elbow [Lemerle et al. \(2019\)](#), [Baggetta et al. \(2022\)](#) and ankle prostheses [Agboola-Dobson et al. \(2019\)](#), and motor rehabilitation devices [Liu et al. \(2018\)](#), [Chen et al. \(2021\)](#), exploiting their affinity with the human musculoskeletal system. However, there still is a lack of fully actuated 3 DoFs wrist joints with variable stiffness.

This work presents a novel and compact VS wrist with 3 DoFs (shown in Figure 1) that can actively vary its overall stiffness with continuity. Thanks to its anthropomorphic characteristics, it holds potential applications in prosthetics and humanoid robotics. This paper extends the mathematical model of a concept already introduced in [Lemerle et al. \(2021\)](#) and [Lemerle \(2021\)](#), validating the efficacy of the idea through the first hardware implementation. Section 2 explains the general design concept of the device, and Section 3 describes its model. Section 4 focuses on the elastic transmission mechanism, describing its working principle and mathematical model. A detailed report of the hardware implementation follows in Section 5. Section 6 depicts the employed control strategy, and Section 7 details the system calibration. Section 8 reports the experimental performance evaluation with a Motion Capture system and showcases practical applications of the device. Finally, Section 9 discusses the experimental results and the applicability of the presented architecture in prosthetics, while conclusions are drawn in Section 10.

2 Design Concept

The VS-Wrist features a hybrid serial-parallel architecture leveraging the redundancy of the actuation system and a non-linear elastic transmission to adjust the stiffness of the coupler. It comprises a 2 DoFs VS joint achieved through a Parallel Manipulator (PM) architecture complemented by an independent serial motor unit that is decoupled from the variable stiffness mechanism.

Figure 2a shows the overall architecture of the 2 DoFs VS joint. As discussed in Lemerle et al. (2021), its leg kinematics draws inspiration from the Omni-Wrist III outlined in Rosheim and Sauter (2002). However, the proposed design incorporates only three legs instead of four, and introduces substantial differences in the actuation system to enable the modulation of joint stiffness. Precisely, the 2 DoFs VS joint integrates a supplementary actuator and a non-linear elastic mechanism in its design to transmit the motion of each motor to the first joint of each kinematic chain.

Figure 2b showcases the mechanical design of the VS-Wrist and delineates its DoFs. In this regard, the PM manages the radial/ulnar deviation (RUD) and the flexion/extension (FE) of the wrist, while the serial motor unit actuates the device along the pronation/supination (PS) axis. Unlike the human wrist, this latter motor unit only rotates the hand, rather than the entire forearm.

The VS-Wrist boasts an innovative mechanical structure that embodies part of the system intelligence. Typically, an n DoFs VS joint would necessitate $2n$ motors to control its position and stiffness. By utilizing a PM, it becomes possible to modulate joint stiffness using internal torques, requiring only three motors to control two positional DoFs and leaving one DoF dedicated to overall stiffness regulation. Consequently, the PM architecture achieves a two DoFs VS joint with the minimum possible number of motors, resulting in a compact and lightweight device. This design choice aligns with the human mechanism of muscular impedance regulation, where muscular cocontraction predominantly modulates the compliance ellipsoid dimensions, while the orientation of its axes essentially depends on posture Ajoudani et al. (2018), Lemerle et al. (2021).

3 System Analysis

To investigate the behavior of the device, we commence the kinematic analysis by considering the PM alone. Subsequently, we incorporate the effect of the serial motor unit, given that its rotation does not impact the PM kinematics. We define the reference coordinate frame $\{S_b\} = \{O_b, X_b, Y_b, Z_b\}$, fixed to the base of the wrist, and $\{S_e\} = \{O_e, X_e, Y_e, Z_e\}$, attached to the coupler. As shown in Figure 4, their origins (O_b and O_e) are located at the center of the base and coupler, respectively. The X -axes point upwards, the Z -axes point to the right, and the Y -axes are determined by the right-hand rule. The pose of the end-effector with respect to (w.r.t.) the fixed frame $\{S_b\}$ can be parametrized by the vector $\mathbf{x} = [\alpha_x \ \alpha_y \ \alpha_z \ x_e \ y_e \ z_e]^T$, whose first three components represent Euler angles, while the last three defines the position of O_e . However, since the PM has 2 DoFs, the minimum parametrization $u = [\alpha_y \ \alpha_z]^T$, representing the

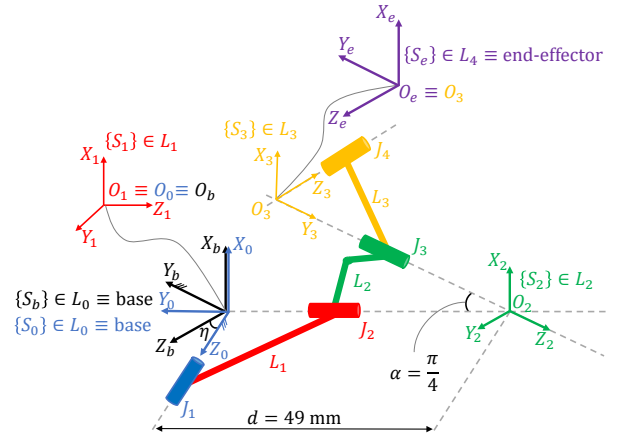


Figure 3. Definition of the local reference coordinate frames of a generic leg according to the Denavit Hartenberg convention. d , η , and α are fixed design parameters.

Table 1. Denavit Hartenberg parametrization of a generic leg of the PM. $d = 49$ mm, $\alpha = \frac{\pi}{4}$ are fixed design parameters.

$\{S_{i-1}\} \rightarrow \{S_i\}$	θ_i	d_i	a_i	α_i
$\{S_b\} \rightarrow \{S_0\}$	0	0	0	η
$\{S_0\} \rightarrow \{S_1\}$	q_1	0	0	$\pi/2$
$\{S_1\} \rightarrow \{S_2\}$	q_2	d	0	$-\alpha$
$\{S_2\} \rightarrow \{S_3\}$	q_3	$-d$	0	$\pi/2$
$\{S_3\} \rightarrow \{S_e\}$	q_4	0	0	$\pi - \eta$

RUD and the FE angles of the wrist, is sufficient to uniquely determine its pose.

We define the homogeneous transformation matrices $T_{T_*}(p)$ and $T_{R_*}(p)$ that encode translation and rotation along the generic $*$ -axis of the quantity p . Consistent with the analysis provided in Lemerle et al. (2021), the matrix $T_b^e(\mathbf{x})$, encoding the pose \mathbf{x} of $\{S_e\}$ w.r.t. $\{S_b\}$, is

$$T_b^e(\mathbf{x}) = \begin{matrix} T_{T_z}(z_e)T_{T_y}(y_e)T_{T_x}(x_e) \\ T_{R_z}(\alpha_z)T_{R_y}(\alpha_y)T_{R_x}(\alpha_x) \end{matrix} \quad (1)$$

The transformation matrix T_b^e can also be derived from the joint angles of a single leg $q = [q_1 \ q_2 \ q_3 \ q_4]^T$. We parametrize each kinematic chain of the manipulator according to the Denavit Hartenberg convention, as shown for a generic leg in Figure 3 and Table 1. The intermediate transformations in local frames are assembled to obtain

$$T_b^e(q) = T_b^0(\eta)T_0^1(q_1)T_1^2(q_2)T_2^3(q_3)T_3^e(q_4) \quad (2)$$

where $T_{i-1}^i = T_{R_z}(\theta_i)T_{T_z}(d_i)T_{R_x}(\alpha_i)T_{T_x}(a_i)$ defines the homogeneous transformation matrix between subsequent local frames. The PS rotation axis is always parallel to the X_e -axis. Therefore, indicating with θ_{PS} the related motor angle, the resulting homogeneous transformation matrix becomes

$$T_b^e(q, \theta_{PS}) = T_b^e(q)T_{R_x}(\theta_{PS}) \quad (3)$$

3.1 Pronation/Supination Transmission Kinematics

The PS motor transmits motion to the end-effector through a kinematic chain featuring two opposed Universal

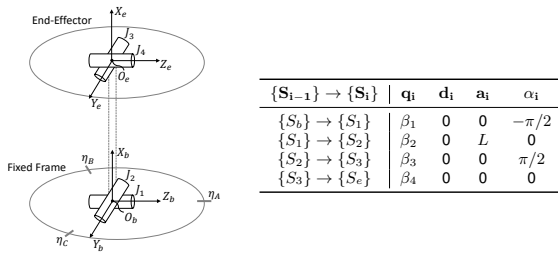


Figure 4. Schematic representation of the PS transmission. Each UJ is represented with two perpendicular and incident revolute joints, positioned at the center of either the fixed base frame or the coupler. Note that the two UJs are 90° out of phase to counteract the changing angular velocity of the driving shaft introduced by the lower UJ. The table on the right summarizes the Denavit-Hartenberg parametrization of the kinematic chain. $L = d\sqrt{2}(1 - \cos(\alpha)) = 37.5$ mm is a fixed design parameter.

Joints (UJs) with rotation centers located at O_b and O_e . Figure 4 illustrates the schematization of the PS kinematic chain and reports its Denavit-Hartenberg parametrization. Therefore, the UJs angles $\beta = [\beta_1 \ \beta_2 \ \beta_3 \ \beta_4]^\top$ parametrize the homogenous transformation matrix from $\{S_b\}$ to $\{S_e\}$ as

$$T_b^e(\beta) = T_b^1(\beta_1)T_1^2(\beta_2)T_2^3(\beta_3)T_3^e(\beta_4). \quad (4)$$

To solve the Inverse Kinematics (IK) of the PS mechanism, we exploit that the position of the coupler is independent of β_3 and β_4 , and thus

$$O_2(\beta_1, \beta_2) = T_b^2(1:3, 4) = T_b^e(1:3, 4) = O_e. \quad (5)$$

Solving (5) yields β_1 and β_2 as

$$\begin{cases} \beta_1 = \text{atan2}(y_e, x_e) \\ \beta_2 = \text{atan2}\left(-z_e, \frac{y_e}{\sin(\beta_1)}\right) \end{cases}. \quad (6)$$

Finally, we equate $T_b^e(\beta_3, \beta_4) = T_b^{2-1}T_b^e$ to find β_3 and β_4 as

$$\begin{cases} \beta_3 = \text{atan2}(T_2^e(1, 3), -T_2^e(2, 3)) \\ \beta_4 = \text{atan2}(T_2^e(3, 1), T_2^e(3, 2)) \end{cases}. \quad (7)$$

Due to the PM kinematics, the angles of the UJs are pairwise equal (i.e., $\beta_3 = \beta_2$ and $\beta_4 = \beta_1$). These findings can be utilized for detecting non-idealities in the PM kinematics or for system calibration purposes.

3.2 Single Leg Forward Kinematics

The transformation matrix $T_b^e(q)$ that encodes the pose of the end-effector w.r.t. $\{S_b\}$ using joint angles q , must be equivalent to $T_b^e(x)$, obtained through the Euler angles parametrization x .

Equating these two matrices and solving for x yields

$$\begin{cases} x_e = T_{1,4}(q) \\ y_e = T_{2,4}(q) \\ z_e = T_{3,4}(q) \\ \alpha_x = \text{atan2}(T_{3,2}(q), T_{3,3}(q)) \\ \alpha_y = \text{atan2}\left(-T_{3,1}(q), \sqrt{T_{3,2}(q)^2 + T_{3,3}(q)^2}\right) \\ \alpha_z = \text{atan2}(T_{2,1}(q), T_{1,1}(q)) \end{cases}, \quad (8)$$

where $T_{i,j}(q)$ denotes the element of the $T_b^e(q)$ matrix at the i th row and j th column. Therefore, given all the joint angles of a single leg, (8) provides the pose of the end-effector w.r.t. the fixed frame $\{S_b\}$.

3.3 Inverse Kinematics

Given the pose of the end-effector x , the IK of the PM yields the joint angles of a given leg. Exploiting the geometrical constraints

$$\begin{cases} q_3 = q_2 + \pi \\ q_4 = -q_1 \end{cases}, \quad (9)$$

that hold for the chosen mounting arrangement of the legs Sofka et al. (2006), and following the procedure detailed in Lemerle et al. (2021), the IK solution is

$$\begin{cases} q_1 = \text{atan2}\left(\frac{x_e(1 - c_\alpha) + (y_e c_\eta + z_e s_\eta)s_\alpha s_2}{d(1 - c_\alpha)(2 - (1 + c_\alpha)c_2^2)}\right) \\ q_2 = \text{acos}\left(\frac{y_e \sin(\eta) - z_e \cos(\eta)}{ds_\alpha}\right) \\ q_3 = q_2 + \pi \\ q_4 = -q_1 \end{cases}, \quad (10)$$

where s_2, c_2 represent $\sin(q_2), \cos(q_2)$, and s_α, c_α represent $\sin(\alpha), \cos(\alpha)$. The reader can find additional mathematical details about the computations in Lemerle et al. (2021). The IK of the PM is subsequently utilized in Section 6.1 to determine the motor reference angles achieving a desired posture u_r .

3.4 Parallel Mechanism Forward Kinematics

By equating the transformation matrices obtained using the joint angles of different legs, it is possible to derive all the joint variables of a single kinematic chain as a function of the sole sensorized joint angles, which are the first ones of each leg. Computing x_e and y_e as functions of the joint angles of alternatively legs A and B yields

$$\begin{cases} T_{1,4}(q_A) = x_e(q_A) = x_e(q_B) = T_{1,4}(q_B) \\ T_{2,4}(q_A) = y_e(q_A) = y_e(q_B) = T_{2,4}(q_B) \end{cases}. \quad (11)$$

Aligning the fixed base frame with the first local frame of leg A (hence $\eta_A = 0, \eta_B = \frac{2}{3}\pi$, and $\eta_C = \frac{4}{3}\pi$) and using (9), it is possible to solve the first equation of (11) to obtain

$$s_{A_2} = \frac{(s_{B_1} - s_{A_1})(1 - c_\alpha) + s_\alpha c_{B_1} s_{B_2}}{s_\alpha c_{A_1}}, \quad (12)$$

where s_{*n}, c_{*n} indicate the sine and cosine of the n -th joint angle of the leg $*$. Substitute (12) into the second equation of (11) to get

$$q_{B_2} = \text{atan2}\left(\frac{\sqrt{2}(s_\alpha t_5 - t_1 \sqrt{h_1 + h_2})}{t_1(1 - t_3 - t_2 c_{\eta_B} + c_{A_1} s_{\eta_B} s_\alpha)}\right), \quad (13)$$

where $t_1, t_2, t_3, t_4, t_5, h_1, h_2 \in \mathbb{R}$ are defined as

$$\begin{cases} t_1 = c_\alpha - 1 \\ t_2 = c_{A_1} c_{B_1} \\ t_3 = 1 + c_{\eta_B} \\ t_4 = c_{A_1}^2 + c_{B_1}^2 \\ t_5 = c_{\eta_B} c_{A_1} s_{B_1} - c_{B_1} s_{A_1} \\ h_1 = t_4 - t_2^2(1 + c_{\eta_B}^2) \\ h_2 = t_1(1 - t_2) - 2t_2 t_3 c_{\eta_B} \end{cases}. \quad (14)$$

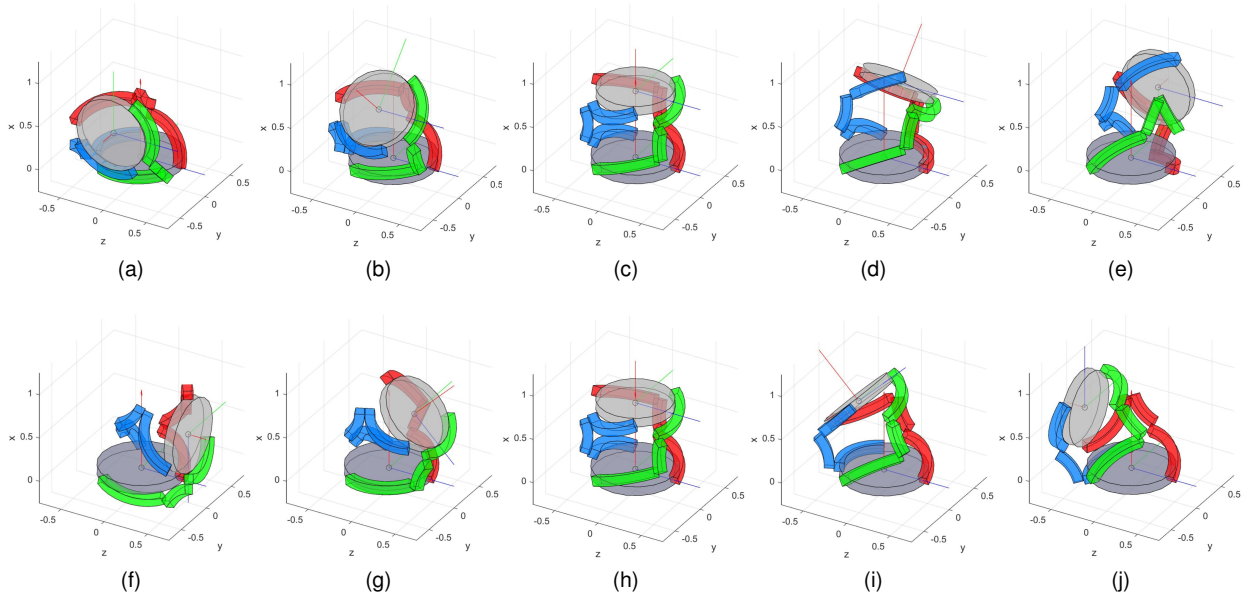


Figure 5. The various panels depict the nominal range of motion of the 2 DoFs VS joint, illustrating the kinematic behavior of the system using the inverse kinematic model. Panels (a) to (e) represent motion around the Y_b -axis, while panels (f) to (j) showcase a revolution around the Z_b -axis (from $\frac{\pi}{2}$ to $-\frac{\pi}{2}$).

Since the encoders measure q_{A_1} and q_{B_1} , (13) and (9) yield all the joint angles of leg B, and (8) provides the pose of the end-effector \mathbf{x} as a function of the sole sensorized variables. This strategy was employed to obtain real-time feedback on wrist posture, and its validation is presented in Section 8.

3.5 Static Equilibrium

To solve the static equilibrium of the PM, we open the kinematic chains at their last joints and impose the equilibrium of the end-effector subject to the external wrench and the reaction forces from the coupling joints. We then enforce the equilibrium of each leg, considering the previously computed reaction forces. This procedure, reported in detail in Appendix A, yields

$$\begin{cases} \tau_a = J_a^\top(q) H^\top(q) \tilde{w} & (15a) \end{cases}$$

$$\begin{cases} \tau_{\bar{a}} = J_{\bar{a}}^\top(q) H^\top(q) \tilde{w} = 0_{9 \times 1} & (15b) \end{cases}$$

$$\begin{cases} w_e = -G(q) H^\top(q) \tilde{w} & (15c) \end{cases}$$

where (15a) expresses the equilibrium of the actuated joints, (15b) defines the balance of the torques on the non-actuated joints (that must be null), and (15c) imposes the equilibrium of the end-effector. As GH^\top is a fat matrix with full row rank, all the possible solutions for (15c) are expressed by

$$\tilde{w} = -(GH^\top)^R w_e + P\Lambda, \quad (16)$$

where $(GH^\top)^R$ is a right-inverse of GH^\top , the columns of P form a basis of the $\ker(GH^\top)$, and Λ is a vector of coefficients that parametrizes the constraint wrenches achieving the static equilibrium of the end-effector. Substituting (16) into (15a) yields

$$\tau_a = -J_a^\top H^\top (GH^\top)^R w_e + J_a^\top H^\top P\Lambda, \quad (17)$$

where Λ must satisfy (15b), leaving only one DoF $\lambda \in \mathbb{R}$ that modulates the internal forces of the 2 DoFs VS joint through the basis $N_0(u)$, defined in Lemerle et al. (2021). Since the actuated torque acting on each leg is a non-linear function of the deflection $\delta = q_1 - \theta_m$ between the first joint and motor angles (i.e., $\tau_a = f(\delta)$), the stiffness of the elastic transmission $K(\delta) = -\frac{\partial \tau_a}{\partial \delta}$ varies with the deflection. Therefore, modulating the internal forces via the parameter λ not only influences the active deflection of the elastic elements but also impacts joint stiffness. This strategy is employed in Section 6.2 to control the stiffness of the device. Solving (15) has been instrumental in sizing the actuation system and computing the maximum load the wrist can manipulate, as reported in Section 9, or determining the range of internal torques achievable with a lower load.

4 Elastic Transmission Mechanism

The elastic transmission mechanism, shown in Figure 6, employs an antagonistic setup of linear springs, tendons, and pulleys to achieve non-linearity thanks to their geometric configuration. To derive the output torque delivered by the elastic transmission, first, we compute the elastic energy stored in the springs as a function of the lever angle γ , obtaining

$$U_s(\gamma) = \frac{1}{2} k (L(\gamma) - L_0)^2, \quad (18)$$

where

$$L(\gamma) = \sqrt{(l_n \sin(\gamma) + d_0)^2 + (l_n(1 - \cos(\gamma)))^2}, \quad (19)$$

is the length of the spring as a function of γ , L_0 is the spring free length, d_0 is its length when $\gamma = 0$, and l_n represents the length of the horizontal lever arm. Then, we differentiate (18) to obtain

$$\tau(\gamma) = -\frac{\partial U_s}{\partial \delta} = -\frac{\partial U_s}{\partial \gamma} \frac{\partial \gamma}{\partial \delta} = -\frac{\partial U_s}{\partial \gamma} \left(\frac{\partial \delta}{\partial \gamma} \right)^{-1}. \quad (20)$$

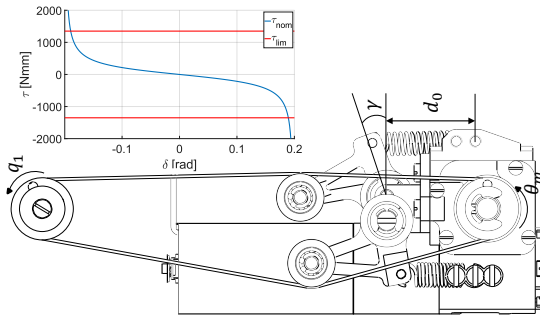


Figure 6. Schematic representation of the non-linear elastic transmission mechanism. The top-left plot depicts the output torque (blue line) as a function of the deflection δ within the nominal range of motor torque (red lines).

The relationship $\delta(\gamma, L_t)$ can be found by imposing the conservation of the tendon length L_t , as outlined in Appendix B. Therefore, given δ from the encoder measurements and assuming L_t is known by design, we can compute γ , and subsequently deduce the actuated torque.

To determine the stiffness of the elastic transmission K , it is sufficient to differentiate (20), yielding

$$K(\gamma) = -\frac{\partial \tau}{\partial \delta} = -\frac{\partial \tau}{\partial \gamma} \left(\frac{\partial \delta}{\partial \gamma} \right)^{-1}. \quad (21)$$

5 Hardware Description

5.1 Mechanical Hardware

Figure 7 shows the CAD of the VS-Wrist along with its overall dimensions. The fixed frame, depicted in red, has a diameter of 70 mm, while the coupler, shown in yellow, has a diameter of 60 mm. The total length of the device is 170 mm, and its weight is 1110 g. These dimensions align with the average sizes of a human wrist and forearm as per NASA (1995) and Damerla et al. (2022).

The VS joint features three identical sides composed of the serial arrangement of a motor unit (in blue), a non-linear elastic transmission (in green), and a kinematic chain of four non-coplanar revolute joints (in magenta). The motor unit comprises a Maxon DCX19S GB KL 12V motor, its associated gearbox, and a low-efficiency worm gear transmission to ensure the non-backdrivability of the system. Thanks to this design choice, the springs can apply constant forces to maintain high stiffness levels or balance static loads without power consumption. The resulting transmission ratio is 420, with an efficiency of 0.28. The maximum continuous torque deliverable to the gearbox output shaft is 1351 Nmm, while the maximum intermittent torque is 3883 Nmm. The nominal power consumption of each motor is 16 W, but since the actuation is non-backdrivable, the power demand is negligible when the wrist is not moving actively.

The kinematic chains, made of aluminum alloy Ergal 7075-T6, evenly distribute around the fixed frame. To assess the robustness of the device, we performed a FEM analysis of the kinematic chains under maximum load conditions. Figure 8 illustrates the magnitude of the displacement and von Mises stress of the first link when static equilibrium is

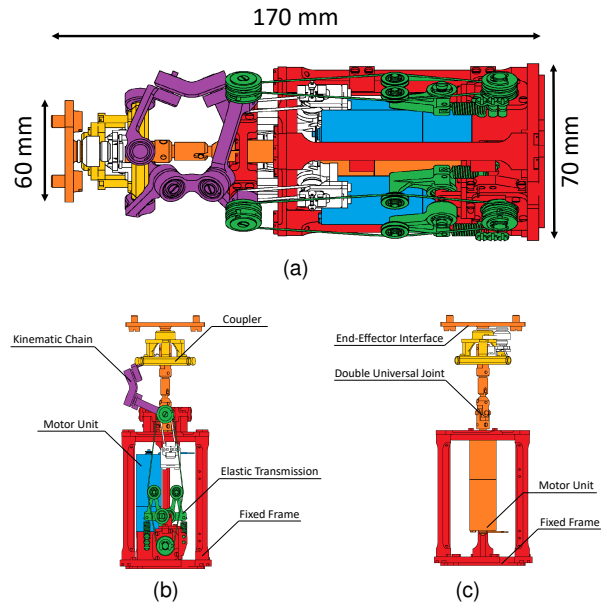


Figure 7. CAD of the VS-Wrist. Each color highlights a different macro-component: red for the fixed frame, blue for the 2 DoFs VS joint motor units, green for the elastic transmission mechanism, magenta for the kinematic chains, orange for the PS unit, and yellow for the coupler. Panel (a) offers a comprehensive 3D view of the device along with its dimensions. Panel (b) details the implementation of one leg and its VS unit, while panel (c) showcases the PS unit.

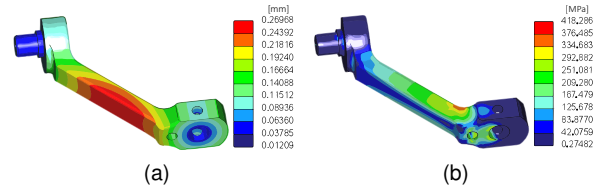


Figure 8. FEM analysis of the first link of the parallel manipulator under maximum load condition. Panel (a) reports the magnitude of the displacement, and panel (b) shows that the von Mises stress remains below the yield strength of the material ($\sigma_Y = 503$ MPa).

reached under an external weight of 5.2 kg. Figure 8a shows that the maximum displacement of the link is restrained and approximately located in the middle section. Figure 8b demonstrates stress concentration in a rounded corner and affirms that the kinematic chain withstands the maximum load condition as the highest stress remains below the yield strength of the material $\sigma_Y = 503$ MPa. The characteristic length $d = 49$ mm and angular deviation $\alpha = \frac{\pi}{4}$ are carefully selected to prevent internal collisions between different legs and attain the desired workspace. The impact of these design parameters on the system workspace and compliance was previously examined in Lemerle et al. (2021). Additionally, Chang-Siu et al. (2022) provides a manipulability analysis assessing wrist dexterity while using a terminal device.

The elastic transmission mechanism achieves VS by adjusting the spring preload. For this purpose, one end of each spring is fixed to the frame, while the other end attaches to the lever arm mechanism that regulates the

tension of the tendons. The elastic elements employed are the extension springs T31320 from MeterSprings, and the tendons are crafted using Liros DC120 from Unlimited Rope Solutions. A traction machine pulled the cables at 90% of their maximum tolerated tension to ensure that their length remains consistent during the regular operation of the wrist.

The PS actuator features a planetary gearbox with a transmission ratio of 168:1, efficiency of 0.65, maximum continuous of 1204 Nmm, maximum intermittent torque of 2000 Nmm, and a power consumption of 16 W. Figure 7c illustrates the mechanical implementation of the PS unit. The double UJ structure compensates for parallel misalignment and non-constant velocities between the driving and driven shafts. Importantly, the transmission is independent of the VS unit, meaning this motor does not modify the stiffness of the joint.

5.2 Electronic Hardware

The device incorporates the NMMI electronics detailed in Della Santina et al. (2017b). Four independent PID controllers regulate the position of the DC motors, relying on feedback from four rotary magnetic encoders that measure the angle θ of the gearbox output shafts. Three additional encoders measure the first joint angle q_1 of each kinematic chain. The 12-bit programmable encoders AS5045 from Austriamicrosystems provide angular positions with a resolution of 0.09° . Four motor drivers MC33887 from NXP Semiconductors independently drive the DC motors. The current flowing to the motor is regulated at 1 kHz by modulating the duty cycle of a 20 kHz PWM signal. The Programmable System-on-Chip (PSoC) 5LP CY8C58LP from Cypress manages the PID controller at a frequency of 1 kHz. The embedded microcontroller is a 32-bit Arm Cortex-M3 core plus DMA. A daisy-chain connection allows various boards to communicate and share power from a single DJI TB47 (4500mAh) battery. The PSoC connects to the computer via micro-USB, and communication is handled through the RS485 serial protocol.

6 Control Architecture

To validate the effectiveness of the proposed hardware without compromising the inherent compliance of the system Della Santina et al. (2017a), we opt for a simple open-loop controller. This control strategy regulates the motor positions based solely on kinematic considerations, remaining independent of the characteristics of the non-linear elastic transmission. The control architecture, schematized in Figure 9, consists of a position controller and a stiffness controller, both decoupled and operating in parallel.

6.1 Posture Control

The posture controller capitalizes on the insight that the system naturally tends towards static equilibrium by minimizing the elastic energy stored in the springs. In the absence of external or internal loads, this equilibrium occurs when the deflection δ is null. Consequently, the angular position of the first joint follows the corresponding motor angle.

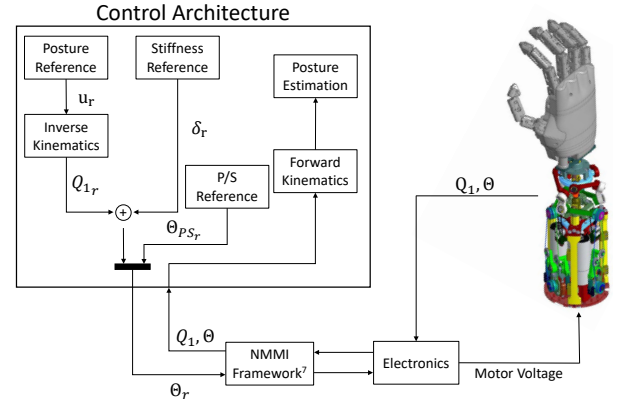


Figure 9. Scheme of the control architecture. A Simulink model sets the position and stiffness references in real-time, communicating with the electronic hardware through the NMMI framework. Bidirectional communication ensures that encoder measurements are available to the user within the Simulink environment.

Given a desired pose of the wrist in minimum parametrization u_r , (10) provides the corresponding first joint angle of each leg $Q_{1r} \in \mathbb{R}^3$. Consequently, the reference position of the motors $\Theta_r^p \in \mathbb{R}^3$, is determined by

$$\Theta_r^p = Q_{1r} = \mathcal{IK}_1(u_r) . \quad (22)$$

Since the serial motor unit directly acts on the PS of the wrist, this DoF is independently regulated using a conventional proportional control loop.

6.2 Stiffness Control

As described in Section 3.5, the internal forces delivered by the actuation system $\tau_s = \lambda N_0(u)$ govern stiffness regulation. Although the base of the actuated internal torques relies exclusively on the kinematics of the manipulator, deriving the motor angles that yield these torques requires perfect knowledge of the elastic transmission model. However, non-modeled phenomena, such as hysteresis, tendon stretching, and manufacturing variability, limit the reliability of the derived model.

For simplicity, we assume all the VS units to be identical, and we neglect the variations of N_0 with posture, considering it constant at the value achieved when the wrist is in the central position. Then, we refine this approximation through a calibration procedure described in Section 7.2. We define the motor references that modulate the stiffness of the coupler $\Theta_r^s \in \mathbb{R}^3$ as

$$\Theta_r^s = \delta_r N_0 = \delta_r \begin{bmatrix} 1 \\ 1 \\ 1 \end{bmatrix} , \quad (23)$$

where $\delta_r \in \mathbb{R}$ represents the desired deflection of each VS unit. Since the output stiffness monotonically increases with δ_r , we adopt this variable as a means to control the stiffness.

6.3 Combined Control

Integrating stiffness and posture control, the device moves to the commanded posture while the VS units maintain

the desired preload. Due to the non-backdrivability of the actuation, external wrenches acting on the wrist do not influence the motor output shaft. As a result, the device consistently displaces according to the commanded stiffness, leveraging the embedded elasticity. To concurrently manage both joint stiffness and position, we assume the two controllers to be perfectly decoupled. Consequently, we define the motor reference angles as:

$$\Theta_r^c = \mathcal{IK}_1(u_r) + \delta_r \begin{bmatrix} 1 \\ 1 \\ 1 \end{bmatrix}. \quad (24)$$

Finally, a simple proportional control yields the commanded motor angle.

6.4 Hardware Implementation

The hardware implementation of the high-level controller, schematized in Figure 9, was conducted in MATLAB Simulink using the NMMI framework Della Santina et al. (2017b). This setup enables real-time bidirectional communication between Simulink and the electronic components of the VS-Wrist. To account for delays arising from the communication protocol and computations, the frequency of the Simulink diagram was reduced to 200 Hz, ensuring real-time execution.

7 System Calibration and Characterization

We calibrate the system to address errors arising from manufacturing tolerances and other un-modeled phenomena. The limitations of the prototype, stemming from non-nominal behavior, are summarized and discussed in Section 9.1.

7.1 Experimental Setup

We measure the posture of the wrist using a Vicon² motion capture system consisting of 12 optical cameras and 14 reflective markers.

With the aid of custom 3D-printed supports, three sets of markers are affixed to the base frame, the coupler, and the end-effector, respectively (see Figure 10). The camera data are sampled at a frequency of 100 Hz and exported to Matlab for post-processing. Utilizing the marker trajectories, we reconstruct the absolute position and orientation of the reference frames $\{S_b\}$ and $\{S_e\}$ to compute the posture of the end-effector \mathbf{x} , and the transformation matrix $T_b^e(\mathbf{x})$ as in (1). The experimental procedure draws inspiration from Grioli et al. (2015) and Mihcin et al. (2021).

7.2 Stiffness Control Calibration

Although the system can theoretically modulate its stiffness without moving the end-effector, we observe a slight deviation of the coupler when controlling the prototype based on the nominal model (see Figure 11, dashed lines). To address this issue, we fit the experimental data to determine a compensation command that mitigates the observed posture drift using least squares optimization. Subsequently, we adjust the reference posture angles as

$$\begin{cases} \alpha_{yc} = \alpha_{yr} + P_y^4(\delta_r) \\ \alpha_{zc} = \alpha_{zr} + P_z^4(\delta_r) \end{cases}, \quad (25)$$

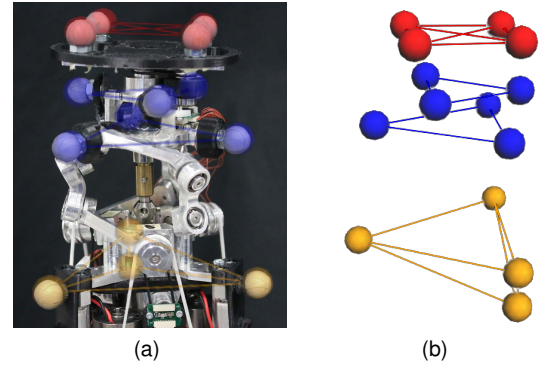


Figure 10. Panel (a) shows the employed marker set, and panel (b) displays its reconstruction conducted by the motion capture system within the Vicon Nexus environment.

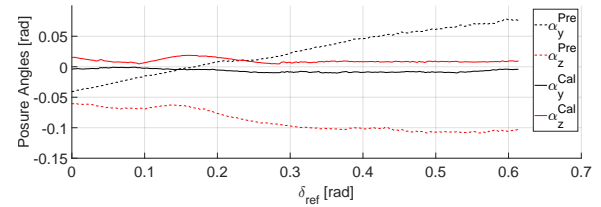


Figure 11. Calibration of the stiffness controller. The graph demonstrates that, prior to calibration, a pure stiffness command induces changes in the wrist posture due to manufacturing variability (dashed lines). Repeating the experiments after applying the compensation command validates that the proposed calibration process effectively mitigated this undesired phenomenon (continuous lines).

where α_{yc}, α_{zc} represent the compensated angles derived from the original references α_{yr}, α_{zr} and $P_y^4(\delta_r), P_z^4(\delta_r)$ are fourth-order polynomials of the variable δ_r that provide the compensation command.

7.3 Combined Control Calibration and Characterization

To characterize the behavior of the posture controller, we begin by testing each DoF separately using step and sine wave posture references. Subsequently, we combine all DoFs to estimate the RoM of the device. Each trial is repeated three times for each of the six tested stiffness configurations.

Figure 12a demonstrates how the device tracks a sinusoidal reference at different stiffness configurations. Notably, the RoM of the device slightly reduces as the stiffness grows. At maximum stiffness, the device achieves ± 0.85 rad for α_y , and $[-0.8, 0.9]$ rad for α_z . The proportional controller provides swift and accurate pursuit of motor reference, with an average $RMSE(\theta) = 0.02$ rad. However, the effective posture of the prototype deviates from the sinusoidal reference by approximately 40% ($RMSE(u) = 0.35$ rad), exhibiting undesired cross-axis movements.

We sampled the 2D-RoM of the VS joint with a grid and acquired static measurements of the device posture, combining movements on both planes at various stiffness configurations. Figure 12b portrays the RoM of the prototype along the FE and RUD DoFs, showing that the workspace

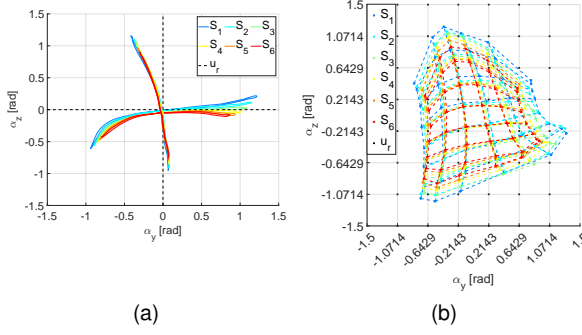


Figure 12. Characterization of the kinematic behavior of the device. Each color represents a different stiffness configuration (increasing from S_1 to S_6). Panel (a) shows the device tracking sinusoidal references, acting on a single axis per time. Panel (b) shows the experimental RoM of the prototype obtained by sampling its 2D workspace with a grid.

of the device is smaller than the nominal one and reduces as the stiffness of the wrist increases. The average standard deviation of the posture among different repetitions of the same trial is very low ($\sigma_u = 0.04$ rad), indicating precise and reproducible control. However, accuracy is compromised ($RMSE(\alpha_y) = 0.25$ rad, $RMSE(\alpha_z) = 0.50$ rad) due to the use of open-loop control based on the nominal model, resulting in significant discrepancies between the actual and controlled positions.

Based on the identified kinematic behavior, we developed a linear map that adjusts the posture reference by leveraging experimental data. Given a desired posture $\bar{u} = [\bar{\alpha}_y \ \bar{\alpha}_z]^\top$ within the RoM of the device, we sample its four neighbors $\mathbb{U}_4^N(\bar{u})$ on the feedback posture grid. Subsequently, we compute a weighted average of their corresponding command to obtain

$$\bar{\alpha}_*^c = \sum_{i=1}^4 \left(\frac{w_{*i}}{\sum_{i=1}^4 w_{*i}} \frac{\bar{\alpha}_*}{\alpha_{*i}} \bar{\alpha}_{*i} \right) \quad \text{for } * = y, z, \quad (26)$$

where $\alpha_{*i} \in \mathbb{U}_4^N(\bar{u})$ represents a neighbor sampled on the experimental grid, $\bar{\alpha}_{*i}$ denotes its associated commanded posture, $w_{*i} = (\alpha_{*i} - \bar{\alpha}_*)^{-2}$ weights its distance from the desired posture, and $\bar{u}^c = [\bar{\alpha}_y^c \ \bar{\alpha}_z^c]^\top$ is the compensated posture reference. We account for the variability of the kinematic behavior with the stiffness by computing \bar{u}^c on the two grids whose stiffness is the closest to the reference configuration and then performing a weighted average of the results based on the difference in stiffness from the desired one.

7.4 Posture Reconstruction Calibration

We evaluated the accuracy of the posture reconstructed by the encoders along the grid, considering the measurements of the motion capture system as ground truth. The previous experiment demonstrated that the posture along one DoF is influenced by the posture along the other and the stiffness. Therefore, we adapted the method in Iosa et al. (2014) by using multivariate linear regression to fit the measurements

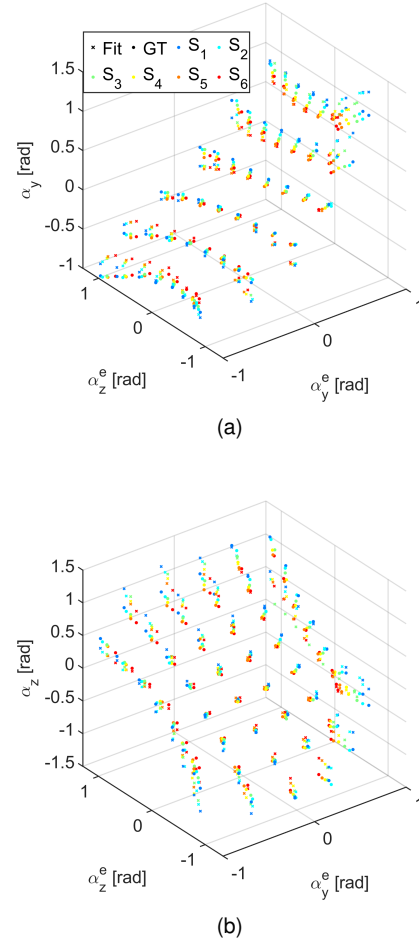


Figure 13. Wrist posture reconstructed through multivariate linear regression. Each color corresponds to a distinct stiffness configuration (increasing from S_1 to S_6). Crosses indicate the posture reconstructed by the algorithm, while dots represent the posture measured with motion capture, assumed as the ground truth.

Table 2. Coefficients and statistics from the multivariate linear regression used to estimate wrist posture. Inside the parentheses is reported the 95% confidence interval of the estimated parameters.

α_*	p_{*0}	p_{*y}	p_{*z}	p_{*s}	$RMSE$	R^2
α_y	0.06 (0.03, 0.09)	0.91 (0.89, 0.94)	-0.15 (-0.18, -0.14)	-0.09 (-0.17, -0.01)	0.12	0.96
α_z	-0.03 (-0.08, 0.01)	0.15 (0.11, 0.18)	0.75 (0.72, 0.78)	-0.08 (-0.21, 0.04)	0.18	0.90

of the motion capture system as

$$\begin{cases} \alpha_y^{GT} = p_{y0} + p_{yy}\alpha_y^e + p_{yz}\alpha_z^e + p_{ys}\delta_r + \varepsilon_y \\ \alpha_z^{GT} = p_{z0} + p_{zy}\alpha_y^e + p_{zz}\alpha_z^e + p_{zs}\delta_r + \varepsilon_z \end{cases} \quad (27)$$

where α_*^{GT} represents the posture along the $*$ -axis measured with the motion capture, α_*^e is the posture reconstructed by using the encoders and neglecting any secondary interaction, p_{*i} are the identified linear coefficients that fit the data, and ε_* is the residual of the fit. Table 2 and Figure 13 report the output of the estimation. Note that R^2 is close to 1,

indicating a significant fit. Moreover, the bias coefficients p_{*0} are close to 0, and the direct proportional coefficients p_{yy} and p_{zz} are close to 1, suggesting that α_*^e is accurate. Still, we could improve the estimate by exploiting the additional information about the dependency of the pose from the stiffness and the second DoF.

8 Experimental Validation

To validate the control strategy, we replicated the experiments detailed in Section 7 after applying the calibration procedure.

Figure 14a reports the posture of the device while chasing sinusoidal references acting, one per time, on both DoFs. To assess the accuracy of the posture pursuit, we applied the Linear Fit Method (LFM) as in Iosa et al. (2014). Precisely, we fit the posture reference with a linear model of the effective posture. Consequently, if the tracking is accurate, the linear coefficient will be close to 1 and the bias close to 0. The results of the linear fit, resumed in the upper half of Table 3, confirmed that the posture of the device is an accurate replica of the desired pose. Additionally, we applied the LFM to compare the posture estimated using the encoders with the measurements of the motion capture system. The results, presented on the right side of Table 3, confirmed that the posture is reconstructed accurately.

Figure 14b shows the performance of the VS joint tracking simultaneous references on both axes. Similarly, we applied the LFM to evaluate the accuracy of posture tracking and estimation. The identified parameters, reported in the lower half of Table 3, affirmed the effectiveness of the calibration procedure, validating both posture control and reconstruction strategies. Notably, the experimental data did not reveal any correlation between the commanded stiffness and posture tracking and reconstruction performance or the workspace.

The PS unit achieves very precise ($\sigma_{PS} = 0.01$ rad) and accurate control ($RMSE(\theta_{PS}) = 0.02$ rad), and its RoM is unconstrained ($\pm\pi$).

The output speed of the device is computed using step references that span the RoM of each individual DoF at minimum and maximum stiffness configurations. The wrist speed decreases as the stiffness increases, except for the PS, as its mechanical transmission is decoupled from the VS units. The average output speed ranges from 4.0 to 8.4 rad/s for the FE and from 3.0 to 6.3 rad/s for the RUD, while the PS average speed is 10.8 rad/s.

8.1 Variable Stiffness Ability

The VS-Wrist exploits its redundant elastic actuation to vary the stiffness of the coupler, adapting to tasks of different natures. To demonstrate this capability, we replicated the experiment depicted in Figure 12b after attaching a load to the end-effector. During this experiment, the VS-Wrist is hung upside-down on a fixed frame, as shown in Figure 15. An external load of 640 g is affixed to the coupler at a distance of 78 mm. Therefore, the force of gravity applies a known external wrench that varies with the posture of the wrist. To quantify the stiffness, we assume that it remains constant during each trial. This assumption holds

$$\Delta w_u = K_u \Delta u, \quad (28)$$

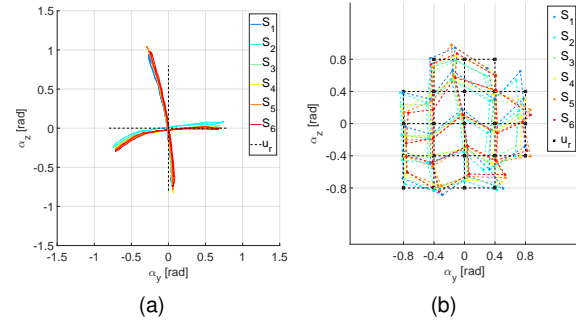


Figure 14. Characterization of the device kinematic behavior after system calibration. Each color corresponds to a distinct stiffness configuration (increasing from S_1 to S_6). Panel (a) shows the device chasing sinusoidal references, acting on a single axis at a time. Panel (b) shows the experimental RoM of the prototype, acquired by sampling its 2D workspace with a grid.

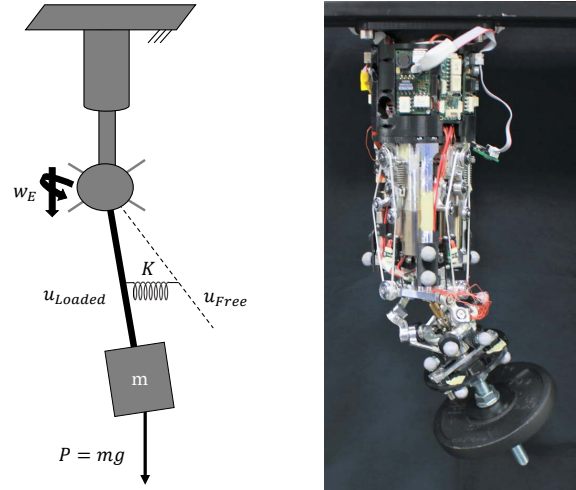


Figure 15. Experimental setup employed to quantify the variable stiffness ability of the device. The VS-Wrist is suspended upside-down from a fixed frame, with a mass attached to the coupler. The external load causes the coupler to shift its equilibrium configuration coherently with the commanded stiffness, exploiting the embedded elasticity.

where $\Delta w_u, \Delta u \in \mathbb{R}^{2 \times N_{sample}}$ are matrices whose columns contain, for each sample of the trial, the difference between the loaded and unloaded condition of the external wrench and posture, respectively, along the minimum parametrization u , and K_u represents the angular stiffness of the device. Therefore, inverting (28) yields the stiffness matrix K_u that best fits the experimental data. Table 4 reports the range of joint stiffness and the statistical significance of its estimation.

Figure 16b shows the device tracking circular trajectories under both loaded and unloaded conditions at various stiffness configurations. The device stiffness dictates its response to external perturbations, with higher stiffness resulting in smaller differences between trajectories in loaded and unloaded configurations. Accordingly, in Figure 16b, the circles reduce their size inversely proportional to the commanded stiffness when the load is applied.

Table 3. Validation of posture control and reconstruction using the LFM. a_* denotes the linear parameter of the LFM and b_* the bias. Data for both sinusoidal and grid references are presented separately for both posture control and reconstruction. The standard errors of the identified coefficients are reported within the parentheses.

Parameter	Posture Control				Posture Reconstruction			
	a_*	b_*	$RMSE$	R^2	a_*	b_*	$RMSE$	R^2
Sinusoidal Reference								
α_y	1.01 (1.4e-3)	0.04 (5.0e-3)	0.08	0.95	1.01 (1.4e-3)	0.05 (4.8e-4)	0.08	0.95
α_z	0.88 (1.3e-2)	0.01 (5.0e-3)	0.08	0.94	0.84 (1.6e-3)	-0.05 (6.6e-4)	0.11	0.91
Grid Reference								
α_y	0.98 (0.01)	-0.02 (5.7e-3)	0.06	0.98	1.03 (0.02)	3.7e-3 (8.2e-3)	0.09	0.97
α_z	0.92 (0.02)	-0.02 (0.01)	0.12	0.940	0.94 (0.03)	-4.0e-3 (0.02)	0.18	0.88

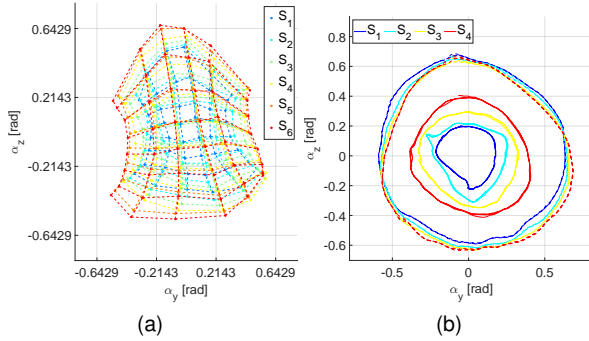


Figure 16. Experimental evaluation of the device variable stiffness ability. Panel (a) reports the posture of the VS joint as it explores its 2D-RoM at various stiffness configurations (increasing from S_1 to S_6) while a load is attached to the end-effector. Panel (b) shows the device tracking circular trajectories at four different stiffness levels (increasing from S_1 to S_4) in both unloaded (dashed lines) and loaded (continuous lines) configurations. The radii of the latter circles are proportional to the stiffness, which defines the resistance to external perturbations.

Table 4. Stiffness range of the device, statistic significance of the fit, and comparison with human wrist stiffness (extracted from Pando et al. (2014)). The stiffness matrix coefficients are reported in Nm/rad and the $RMSE(\Delta w)$ in Nm. Results are reported for the minimum and maximum stiffness configurations, denoted as S_m and S_M . The standard deviation of the estimated coefficients is indicated within the parentheses.

Parameter	S_m	S_M	Human
K_{yy}	0.27 (0.01)	0.93 (0.04)	2.02 (0.19)
$K_{yz} = K_{zy}$	-0.35 (0.02)	-0.51 (0.05)	-0.27 (0.04)
K_{zz}	0.24 (0.01)	0.72 (0.04)	0.85 (0.07)
$RMSE(\Delta w)$	0.03	0.05	
R^2	0.94	0.91	0.98

8.2 Qualitative evaluation of Motion and Stiffness Behavior

To provide a more intuitive representation of the device operating principle and emphasize its anthropomorphism, we map the posture and stiffness of a human operator's wrist into command signals for the robotic device. The reference posture is captured with cameras through a marker set attached to the user's forearm and hand. Furthermore, we registered the operator's myoelectric activity of the wrist flexor and extensor to measure their cocontraction,

which we related to the desired stiffness of the VS-Wrist, similarly to Capsi-Morales et al. (2020). To do so, we employed two commercial electrodes 13E200 from Ottobock, which are commonly used to control prosthetic limbs. Figures 17 and 18 summarize the outcome of the experiments with some frames of the video attached as supplemental material to this paper. Figure 17 shows that the spring preload is modulated through muscular cocontraction while the device tracks the operator's wrist posture. Figure 18 proves that different stiffness configurations achieve various responses to external perturbations. Therefore, the variable stiffness should enhance task adaptability and environmental interactions.

9 Discussion

The initial experimental phase revealed non-idealities, that we addressed and mitigated through a calibration process. The calibration of the stiffness controller, compensating for VS unit asymmetry, successfully eliminated undesired movements associated with changes in joint stiffness. The combined control calibration enhanced posture accuracy by leveraging the experimental motion behavior, identified through grid sampling of the RoM. Undoubtedly, the absence of posture feedback within the control law induces a residual error in the end-effector trajectory. Conversely, our decision to prioritize a simple implementation not only maintains the intrinsic compliance of the device but also demands low computational power, making it well-suited for prosthetic applications. Moreover, the inaccuracy in tracking a desired posture becomes a minor concern in applications where a human operator closes the control loop, such as prosthetics or teleoperation.

The experimental evaluation confirmed that the VS-Wrist can achieve 3 DoFs in position while continuously changing its overall stiffness. Accurate real-time posture reconstruction was achieved using measurements of the first joint angles and forward kinematics. Furthermore, Figure 17 highlights that the VS-Wrist functioning resembles human motion and impedance regulation principles. Although the concept of adaptively controllable impedance in prostheses dates back to the early eighties Hogan (1983), its practical implementation has been hampered by technological limitations. Table 5 compares the features of the VS-Wrist with those of the human and other 3 DoFs prosthetic wrists. The theoretical output torque is sufficient to manipulate a load of 1.8 kg with nominal motor torques and of 5.2 kg

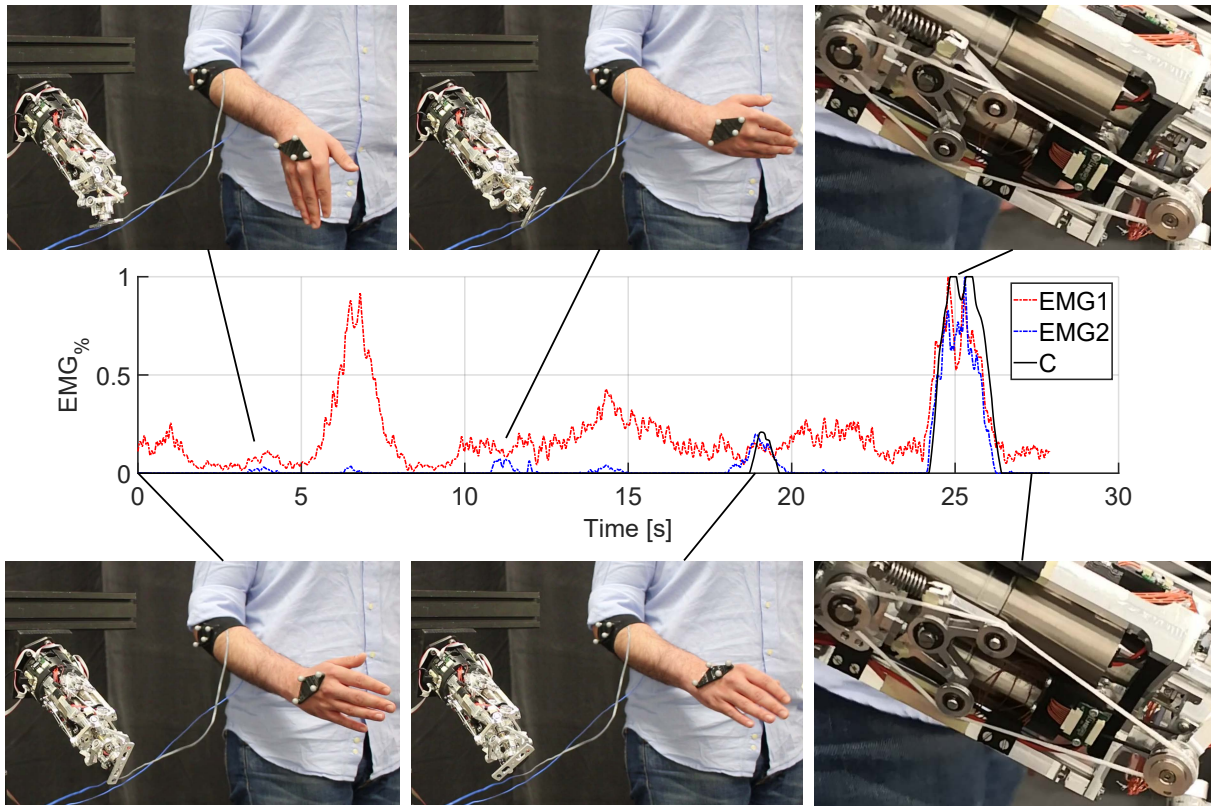


Figure 17. Photosequence capturing the VS-Wrist tracking the user's posture and muscular cocontraction. The central graph displays the corresponding normalized EMG signals measured from a couple of antagonistic muscles of the user's forearm, highlighting the muscular cocontraction C, which defines the stiffness reference of the robotic wrist. Each panel depicts a specific instant of the experiment and is associated with the corresponding EMG measurement. The panels on the right describe the functioning of the elastic transmission that achieves stiffness regulation. The bottom-right frame shows the device in the soft configuration, where tendon tension is low. The top-right panel portrays the VS-Wrist in the rigid configuration, matching the operator's muscular impedance. Coherently, the tendons on one side of all VS units stretch to increase the stiffness.

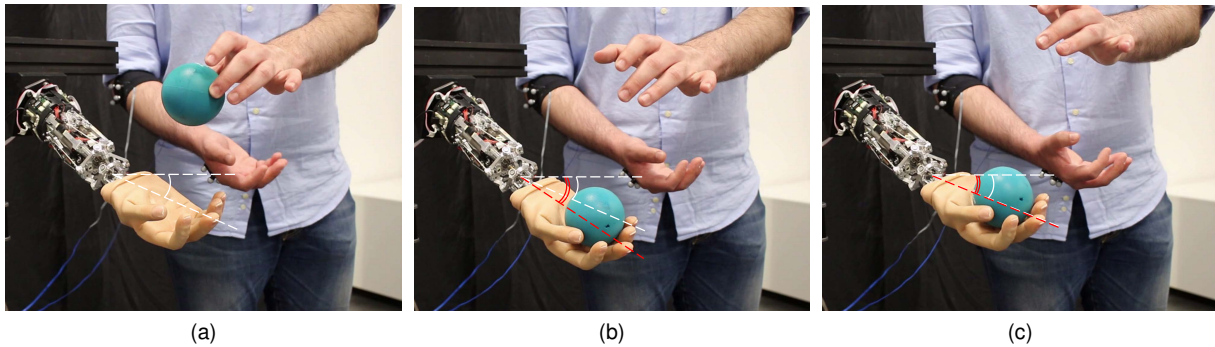


Figure 18. Response to external perturbation at different stiffness configurations. Visual feedback is provided by the angle formed between the segment from the center of the coupler to the middle finger and the horizontal plane. During the trial, the VS-Wrist holds a reference posture (panel (a), white lines) before being impacted by a ball in free fall. Due to variable stiffness, the device reaches different equilibrium configurations (red lines), as illustrated in panel (b) for the soft configuration and (c) for the rigid one.

with maximum motor torques. Note that, due to the non-backdrivability of the actuation system, active motor torque is required only to move from the equilibrium condition, while static loads are counteracted by the friction-based mechanism. The VS-Wrist speed and RoM align with the functional needs of the human wrist. Additionally, its size and weight are smaller than those of the human forearm and are comparable to other 3 DoFs architectures documented in

the literature. Despite these similarities, our first prototype presents limitations hindering its prosthetic application.

9.1 Prototype Limitations

We expect several mechanical refinements for the next release of the prototype. The current version exhibited limitations in both maximum payload and stiffness, primarily

Table 5. Comparative table showcasing human and 3 DoFs prosthetic wrists. Apart from the VS-Wrist, all the other devices feature rigid and fixed impedance actuation. This table has been adapted from [Damerla et al. \(2022\)](#). The tested RoM of the prosthetic devices is reported inside square brackets. Cells are left empty when information is missing at the source.

Name	DoFs	RoM (°)	D (mm)	L (mm)	m (g)	τ (Nm)	ω (rad/s)
Median Male Wrist and Forearm	PS	83/100 (61/75)*	98	269	1420	9/9.5	38/33
	FE	76/73 (54/48)*				12.7/7.9	27/26 (1.7)*
	RUD	25/45 (22/38)*				13.0/12.4	10/11 (1.7)*
Median Female Wrist and Forearm	PS	83/100 (61/75)*	86	243	1060	4.5/4.6	38/33
	FE	76/73 (54/48)*				8.8/5.8	27/26 (1.7)*
	RUD	25/45 (22/38)*				8.2/8.0	10/11 (1.7)*
VS-Wrist	PS	360+	70	170	1110	2	10.8
	FE	90/90 [55/45]				2.4	4-8.4
	RUD	90/90 [48/48]				2.7	3-6.3
Bajaj and Dollar (2018)	PS	360+	86	180	578		1.84
	FE	90/90 [\geq 40/40]					\geq 0.6
	RUD	90/90 [\geq 40/40]					\geq 0.6
Abayasiri et al. (2017)	PS	[70/85]		182	3200 Total for Hand, Wrist, Elbow		
	FE	[60/60]					
	RUD	[25/27]					
Fite et al. (2008)	PS	150			2000 Total for Hand, Wrist, Elbow	4.2	
	FE	170				4.5	
	RUD	60				4.5	

* Functional for standard activities of daily living.

attributed to high manufacturing tolerances resulting in mechanical backlashes. For this reason, attempts to replicate experiments detailed in Section 8.1 with the wrist positioned horizontally were unsuccessful. The device could only sustain the payload at high stiffness levels and within a limited RoM, precluding the identification of its stiffness. Additionally, despite incorporating the functional RoM of the human wrist, the prototype workspace and accuracy were reduced due to non-nominal kinematics.

Although the VS-Wrist approximately matches half the size and weight of a human forearm, future designs should optimize its weight for enhanced user comfort. Furthermore, the prototype length may pose challenges in fitting most transradial amputees but could be suitable for transhumeral amputees.

As this paper presents our first prototype, certain aspects require refinement in both design and manufacturing before undergoing clinical trials. Nonetheless, with proper optimization, the proposed architecture holds promise for prosthetic applications, introducing innovative features such as variable stiffness and 3 DoFs movements. This makes it a significant contribution to the field of prosthetics, as the presented design has the potential to considerably enhance the dexterity and naturalness of upper limb prostheses, addressing the limitations of current commercial devices that predominantly feature passive, rigid joints with restricted DoFs.

10 Conclusion and Future Developments

This study addresses the challenge of modeling and controlling a variable stiffness 3 DoFs wrist featuring redundant elastic actuation. Its controllable stiffness and inherent compliance enable the device to interact safely with the environment, adapting to tasks of various natures. In the soft configuration, contact forces are minimized, while

the device effectively resists external perturbations at high stiffness. The presented calibration procedure successfully compensated for the prototype deviations from its nominal model, ensuring precise posture control and reconstruction.

Optimizing the design and manufacturing processes is crucial to reduce mechanical backlash and augment the stiffness of the device. Attention must be directed towards minimizing the device weight, considering the potential discomfort for prosthesis users. Additional investigations into the robustness of the device are necessary to ensure proper functionality during extended use. Nevertheless, the VS-Wrist holds the potential to enhance the natural feel of existing bionic limbs by resembling the kinematic and compliant behaviors of its natural counterpart. Further quantitative analyses involving standard daily activities could provide valuable insights into assessing the morphological and functional similarities between the device and the human wrist.

Other developments of this work concern the mapping of user EMG signals into control commands for the prosthesis. While coordinated control of multiple DoFs remains an open challenge, recent advancements in neuroscience offer potential solutions for operating more complex prostheses.

Acknowledgements

The authors would like to thank Vinicio Tincani, Mattia Poggiani, Manuel Barbarossa, Emanuele Sessa, Marina Gnocco, Giovanni Rosato, and Anna Pace for their fundamental technical support given during the hardware implementation of this work. An additional thanks goes to Simon Lemerle for his work on the design concept of the device.

Declaration of conflicting interests

The authors declare that the research was conducted in the absence of any commercial or financial relationships that could be construed as a potential conflict of interest.

Funding

This research has received funding from the European Union's ERC program under the Grant Agreement No. 810346 (Natural Bionics). The content of this publication is the sole responsibility of the authors. The European Commission or its services cannot be held responsible for any use that may be made of the information it contains.

Supplemental material

The Supplementary Material for this article, containing a video demonstration of the prototype and mathematical details about the static equilibrium equations and the elastic transmission model, can be downloaded from the dedicated section of this website.

Notes

1. Össur, i-Limb Quantum Flexion Wrist, <https://irp-cdn.multiscreensite.com/acf635e2/files/uploaded/Flexion%20Wrist.pdf>. Last Accessed: May 2023.
2. Vicon, Motion Capture System. <https://www.vicon.com/>. Last Accessed: May 2023

References

Abayasiri RAM, Madusanka DK, Arachchige N, Silva A and Gopura R (2017) Mobio: A 5 dof trans-humeral robotic prosthesis. In: *2017 International Conference on Rehabilitation Robotics (ICORR)*. IEEE, pp. 1627–1632.

Agboola-Dobson A, Wei G and Ren L (2019) Biologically Inspired Design and Development of a Variable Stiffness Powered Ankle-Foot Prosthesis. *Journal of Mechanisms and Robotics* 11(4). DOI:10.1115/1.4043603. URL <https://doi.org/10.1115/1.4043603>. 041012.

Ajoudani A, Fang C, Tsagarakis N and Bicchi A (2018) Reduced-complexity representation of the human arm active endpoint stiffness for supervisory control of remote manipulation. *The International Journal of Robotics Research* 37(1): 155–167.

Albu-Schaffer A, Eiberger O, Grebenstein M, Haddadin S, Ott C, Wimbock T, Wolf S and Hirzinger G (2008) Soft robotics. *IEEE Robotics & Automation Magazine* 15(3): 20–30. DOI: 10.1109/MRA.2008.927979.

Archer SL, Dyck AD, Grant RH, Iversen EK, Jacobs JA, Kunz SR, Linder JR and Sears HH (2011) Wrist device for use with a prosthetic limb. US Patent 7,914,587.

Baggetta M, Berselli G, Palli G and Melchiorri C (2022) Design, modeling, and control of a variable stiffness elbow joint. *The International Journal of Advanced Manufacturing Technology* DOI:10.1007/s00170-022-09886-7. URL <https://doi.org/10.1007/s00170-022-09886-7>.

Bajaj NM and Dollar AM (2018) Design and preliminary evaluation of a 3-dof powered prosthetic wrist device. In: *2018 7th IEEE International Conference on Biomedical Robotics and Biomechanics (Biorob)*. IEEE, pp. 119–125.

Bajaj NM, Spiers AJ and Dollar AM (2019) State of the art in artificial wrists: A review of prosthetic and robotic wrist design. *IEEE Transactions on Robotics* 35(1): 261–277. DOI: 10.1109/TRO.2018.2865890.

Blank AA, Okamura AM and Whitcomb LL (2014) Task-dependent impedance and implications for upper-limb prosthesis control.

The International Journal of Robotics Research 33(6): 827–846.

Borzelli D, Cesqui B, Berger DJ, Burdet E and d'Avella A (2018) Muscle patterns underlying voluntary modulation of co-contraction. *PLoS One* 13(10): e0205911.

Capsi-Morales P, Piazza C, Catalano MG, Bicchi A and Grioli G (2020) Exploring stiffness modulation in prosthetic hands and its perceived function in manipulation and social interaction. *Frontiers in Neurobotics* : 33.

Chang-Siu E, Snell A, McInroe BW, Balladarez X and Full RJ (2022) How to use the omni-wrist iii for dexterous motion: An exposition of the forward and inverse kinematic relationships. *Mechanism and Machine Theory* 168: 104601.

Chen B, Wang B, Zheng C and Zi B (2021) Design and simulation of a robotic knee exoskeleton with a variable stiffness actuator for gait rehabilitation. In: *2021 27th International Conference on Mechatronics and Machine Vision in Practice (M2VIP)*. pp. 24–29. DOI:10.1109/M2VIP49856.2021.9665028.

Damerla R, Rice K, Rubio-Ejchel D, Miro M, Braucher E, Foote J, Bourai I, Singhal A, Yang K, Guang H et al. (2022) Design and testing of a novel, high-performance two dof prosthetic wrist. *IEEE Transactions on Medical Robotics and Bionics* 4(2): 502–519.

Della Santina C, Bianchi M, Grioli G, Angelini F, Catalano M, Garabini M and Bicchi A (2017a) Controlling soft robots: balancing feedback and feedforward elements. *IEEE Robotics & Automation Magazine* 24(3): 75–83.

Della Santina C, Piazza C, Gasparri GM, Bonilla M, Catalano MG, Grioli G, Garabini M and Bicchi A (2017b) The quest for natural machine motion: An open platform to fast-prototyping articulated soft robots. *IEEE Robotics & Automation Magazine* 24(1): 48–56.

English C and Russell D (1999) Mechanics and stiffness limitations of a variable stiffness actuator for use in prosthetic limbs. *Mechanism and Machine Theory* 34(1): 7–25. DOI:[https://doi.org/10.1016/S0094-114X\(98\)00026-3](https://doi.org/10.1016/S0094-114X(98)00026-3). URL <https://www.sciencedirect.com/science/article/pii/S0094114X98000263>.

Fan H, Wei G and Ren L (2022) Prosthetic and robotic wrists comparing with the intelligently evolved human wrist: A review. *Robotica* : 1–23.

Firth C, Dunn K, Haeusler MH and Sun Y (2022) Anthropomorphic soft robotic end-effector for use with collaborative robots in the construction industry. *Automation in Construction* 138: 104218.

Fite KB, Withrow TJ, Shen X, Wait KW, Mitchell JE and Goldfarb M (2008) A gas-actuated anthropomorphic prosthesis for transhumeral amputees. *IEEE Transactions on Robotics* 24(1): 159–169.

Grioli G, Wolf S, Garabini M, Catalano M, Burdet E, Caldwell D, Carloni R, Friedl W, Grebenstein M, Laffranchi M et al. (2015) Variable stiffness actuators: The user's point of view. *The International Journal of Robotics Research* 34(6): 727–743.

Haddadin S, Albu-Schäffer A and Hirzinger G (2007) Safety evaluation of physical human-robot interaction via crash-testing. In: *Robotics: Science and systems*, volume 3. Citeseer, pp. 217–224.

Haddadin S, Weis M, Wolf S and Albu-Schäffer A (2011) Optimal control for maximizing link velocity of robotic variable

- stiffness joints. *IFAC Proceedings Volumes* 44(1): 6863–6871. DOI:<https://doi.org/10.3182/20110828-6-IT-1002.01686>. URL <https://www.sciencedirect.com/science/article/pii/S1474667016447087>. 18th IFAC World Congress.
- Hogan N (1983) Prostheses should have adaptively controllable impedance. In: *Control Aspects of Prosthetics and Orthotics*. Elsevier, pp. 155–162.
- Hogan N (1985) Impedance control: An approach to manipulation: Part ii—implementation. *Journal of Dynamic Systems Measurement and Control-transactions of The Asme* 107: 8–16. URL <https://api.semanticscholar.org/CorpusID:85508543>.
- Iosa M, Cereatti A, Merlo A, Campanini I, Paolucci S, Cappozzo A et al. (2014) Assessment of waveform similarity in clinical gait data: the linear fit method. *BioMed Research International* 2014.
- Lemerle S (2021) Soft robotics technologies to enable natural behavior in a novel generation of bionic upper limbs. *Doctoral Thesis, University of Pisa, Pisa*.
- Lemerle S, Catalano MG, Bicchi A and Grioli G (2021) A configurable architecture for two degree-of-freedom variable stiffness actuators to match the compliant behavior of human joints. *Frontiers in Robotics and AI* 8: 614145.
- Lemerle S, Grioli G, Bicchi A and Catalano MG (2019) A variable stiffness elbow joint for upper limb prosthesis. In: *2019 IEEE/RSJ International Conference on Intelligent Robots and Systems (IROS)*. pp. 7327–7334. DOI:10.1109/IROS40897.2019.8970475.
- Liu Y, Guo S, Hirata H, Ishihara H and Tamiya T (2018) Development of a powered variable-stiffness exoskeleton device for elbow rehabilitation. *Biomedical microdevices* 20(3): 1–13.
- Migliore SA, Brown EA and DeWeerth SP (2005) Biologically inspired joint stiffness control. In: *Proceedings of the 2005 IEEE international conference on robotics and automation*. IEEE, pp. 4508–4513.
- Mihcin S, Ciklacandir S, Kocak M and Tosun A (2021) Wearable motion capture system evaluation for biomechanical studies for hip joints. *Journal of Biomechanical Engineering* 143(4): 044504.
- NASA (1995) Man-systems integration standards - volume i. <https://msis.jsc.nasa.gov/Volume1.htm>. Last Accessed: November 2023.
- Osu R, Kamimura N, Iwasaki H, Nakano E, Harris CM, Wada Y and Kawato M (2004) Optimal impedance control for task achievement in the presence of signal-dependent noise. *Journal of Neurophysiology* 92(2): 1199–1215.
- Pando AL, Lee H, Drake WB, Hogan N and Charles SK (2014) Position-dependent characterization of passive wrist stiffness. *IEEE Transactions on Biomedical Engineering* 61(8): 2235–2244.
- Rosheim ME and Sauter GF (2002) New high-angulation omnidirectional sensor mount. In: Ricklin JC and Voelz DG (eds.) *Free-Space Laser Communication and Laser Imaging II*, volume 4821. International Society for Optics and Photonics, SPIE, pp. 163 – 174. DOI:10.1117/12.465912. URL <https://doi.org/10.1117/12.465912>.
- Sofka J, Skormin V, Nikulin V and Nicholson D (2006) Omni-wrist iii - a new generation of pointing devices. part i. laser beam steering devices - mathematical modeling. *IEEE Transactions on Aerospace and Electronic Systems* 42(2): 718–725. DOI: 10.1109/TAES.2006.1642584.
- Tavakoli M and de Almeida AT (2014) Adaptive under-actuated anthropomorphic hand: Isr-soft-hand. In: *2014 IEEE/RSJ International Conference on Intelligent Robots and Systems*. IEEE, pp. 1629–1634.
- Tröbinger M, Jähne C, Qu Z, Elsner J, Reindl A, Getz S, Goll T, Loinger B, Loibl T, Kugler C et al. (2021) Introducing garmin-a service robotics platform to support the elderly at home: Design philosophy, system overview and first results. *IEEE Robotics and Automation Letters* 6(3): 5857–5864.
- von Drigalski F, Tanaka K, Hamaya M, Lee R, Nakashima C, Shibata Y and Ijiri Y (2020) A compact, cable-driven, activatable soft wrist with six degrees of freedom for assembly tasks. In: *2020 IEEE/RSJ International Conference on Intelligent Robots and Systems (IROS)*. pp. 8752–8757. DOI: 10.1109/IROS45743.2020.9341487.
- Yang G, Li B, Zhang Y, Pan D and Huang H (2022) A novel soft wrist joint with variable stiffness. In: Liu H, Yin Z, Liu L, Jiang L, Gu G, Wu X and Ren W (eds.) *Intelligent Robotics and Applications*. Cham: Springer International Publishing. ISBN 978-3-031-13822-5, pp. 346–356.
- Yellewa ME, Mohamed A, Ishii H and Assal SF (2022) Design and hybrid impedance control of a compliant and balanced wrist rehabilitation device. In: *IECON 2022–48th Annual Conference of the IEEE Industrial Electronics Society*. IEEE, pp. 1–6.
- Zongxing L, Wanxin L and Liping Z (2020) Research development of soft manipulator: A review. *Advances in Mechanical Engineering* 12(8): 1687814020950094.

Appendix A: Derivation of the Static Equilibrium Equations

This appendix details the derivation of the static equilibrium equations reported in Section 3.5. To start, we compute the Jacobian matrix $J_P(q)$ of each leg of the manipulator in the coupling point P with the end-effector. These matrices solely depend on the joint variables of the respective leg and relate their joint velocities to the twist of the coupling point. Exploiting the kinetostatic duality, their transpose relates the torques acting on the joints τ with the wrench w_P acting on the coupling point, such that $\tau = J_P^\top(q)w_P$. Employing the Denavit Hartenberg convention, for a revolute joint, the i th column of the Jacobian matrix can be computed as

$$J_P^i = \begin{bmatrix} k_{i-1} \times O_{i-1}P \\ k_{i-1} \end{bmatrix}, \quad (1)$$

where k_{i-1} represents the versor of Z_{i-1} -axis and $O_{i-1}P$ is the distance of the considered point P from the origin of frame $\{S_{i-1}\}$. All geometrical quantities are expressed in the fixed base frame $\{S_b\}$. The position of the coupling point P w.r.t. the local frame $\{S_3\}$ remains constant and is equal to

$$O_0P = T_b^3(q) \begin{bmatrix} 0 \\ 0 \\ r_c \\ 1 \end{bmatrix}, \quad (2)$$

where $r_c = 22.5$ mm is the coupler radius. Similarly, for the subsequent local frames it holds

$$O_iP = O_0P - T_b^i(:, 4) \quad \text{for } i = 1, 2, 3, \quad (3)$$

where $T_b^i(:, 4)$ denotes the fourth column of the transformation matrix, hence the position of O_i w.r.t. the reference frame $\{S_b\}$. Accounting for the equilibrium of the entire manipulator yields

$$\tau = \begin{bmatrix} \tau_A \\ \tau_B \\ \tau_C \end{bmatrix} = \begin{bmatrix} J_P^A(q_A)^\top & 0_{6 \times 4} & 0_{6 \times 4} \\ 0_{6 \times 4} & J_P^B(q_B)^\top & 0_{6 \times 4} \\ 0_{6 \times 4} & 0_{6 \times 4} & J_P^C(q_C)^\top \end{bmatrix} \begin{bmatrix} w_A \\ w_B \\ w_C \end{bmatrix} = J^\top(q)w, \quad (4)$$

where $\tau_* \in \mathbb{R}^4$ represent the joint torques acting on the leg $*$, $w_* \in \mathbb{R}^6$ is the wrench acting on the coupling point of the same leg, and $J^\top(q) \in \mathbb{R}^{12 \times 12}$ is the complete Jacobian of the parallel manipulator. We introduce the matrix G_* which conveys the effect of the wrench w_* acting on P_* , to the center of the end-effector O_e as

$$G_* = \begin{bmatrix} I_{3 \times 3} & 0_{3 \times 3} \\ \widehat{O_eP_*} & I_{3 \times 3} \end{bmatrix}, \quad (5)$$

where $\widehat{O_eP_*}$ is the skew-symmetric matrix that performs the cross product, defined as $\widehat{O_eP_*}v = O_eP_* \times v$. Therefore, given an external wrench acting on the end-effector w_e , and assembling the grasp matrices for all the legs as $G = [G_A \ G_B \ G_C]$, it holds

$$w_e = -Gw. \quad (6)$$

Because of the constraints imposed by the coupling joints, $w_* = H_*^\top \tilde{w}_*$ cannot be arbitrary. The rows of H_* represent a basis for the constraint reaction of the coupling joint. For a coupling revolute joint, since its rotation axis is parallel to $k_3 = T_b^3(1 : 3, 3)$, we obtain

$$H_* = \begin{bmatrix} T_b^3(1 : 3, 1 : 3)^\top & 0_{3 \times 3} \\ 0_{2 \times 3} & T_b^3(1 : 3, 1 : 2)^\top \end{bmatrix}, \quad (7)$$

where the first three columns of $T_b^{3^\top}$ contain the cartesian components of $\{S_3\}$ versors expressed in $\{S_b\}$. Similarly, the matrix that accounts for the constraints of every leg is

$$H = \begin{bmatrix} H_A & 0_{5 \times 6} & 0_{5 \times 6} \\ 0_{5 \times 6} & H_B & 0_{5 \times 6} \\ 0_{5 \times 6} & 0_{5 \times 6} & H_C \end{bmatrix}. \quad (8)$$

Therefore, the static equilibrium of the parallel manipulator holds

$$\begin{cases} \tau = J^\top H^\top \tilde{w} \\ w_e = -GH^\top \tilde{w} \end{cases} \quad (9a) \quad (9b)$$

Since the system is underactuated, it is possible to act directly only on some joints of the manipulator. Therefore, it is convenient to apply a change of base to (9a) that reorders the joint torques τ , separating the balance on the actuated torques τ_a from the non-actuated ones $\tau_{\bar{a}}$, as

$$\begin{bmatrix} \tau_a \\ \tau_{\bar{a}} \end{bmatrix} = \begin{bmatrix} B_a \\ B_{\bar{a}} \end{bmatrix} \tau = B\tau, \quad (10)$$

where

$$B_a = \begin{bmatrix} 1 & 0 & 0 & 0 & 0 & 0 & 0 & 0 & 0 & 0 & 0 & 0 \\ 0 & 0 & 0 & 0 & 1 & 0 & 0 & 0 & 0 & 0 & 0 & 0 \\ 0 & 0 & 0 & 0 & 0 & 0 & 0 & 0 & 1 & 0 & 0 & 0 \end{bmatrix} \quad (11)$$

and $B_{\bar{a}}$ completes the orthonormal basis. Finally, left-multiplying (9a) by the change of base matrix B yields the system of equations (15).

Appendix B: Derivation of the Elastic Transmission Congruence Equation

This appendix describes the approach employed to derive the model of the elastic transmission mechanism, reported in Section 4. We derive the function $\delta(\gamma)$ by equating the tendon length L_t , known by design, with the same length computed as a function of the geometry of the mechanism (see Figure 1), the deflection δ , and the lever angle γ .

Define the centers of the output motor shaft O_m , the fixed lever pulley O_t , the first joint of the parallel manipulator O_P , and the mobile pulley O_G . The winding angle is defined as the angle formed by the normal versor at the contact point of the tendon on the pulley with the fixed horizontal reference. While O_m , O_P , and O_t remain constant and are known by design, the position of O_G depends on γ as

$$O_m O_G(\gamma) = O_m O_t + b \begin{bmatrix} \cos(\gamma + \alpha_0) \\ \sin(\gamma + \alpha_0) \end{bmatrix}, \quad (12)$$

where $b = 18$ mm represents the length of the oblique lever arm and $\alpha_0 = 70.6^\circ$ is the interior angle it forms with the horizontal arm. By defining the radius of the motor and joint pulleys R_P and that of the mobile pulley as r_G , the length of segment BC is

$$BC(\gamma) = \sqrt{|O_m O_G|_2^2 - (R_P - r_G)^2}, \quad (13)$$

and the angles ψ_l and ψ_l^i are

$$\psi_l = \arccos\left(\frac{(O_m O_G)_x}{|O_m O_G|_2}\right), \quad \psi_l^i = \arcsin\left(\frac{BC}{|O_m O_G|_2}\right). \quad (14)$$

Therefore, the winding angle on the lower side of the mobile pulley β_l is their difference $\beta_l = \psi_l^i - \psi_l$. Similarly, compute the winding angle for the upper side of the mechanism, starting from

$$O_P O_G(\gamma) = O_P O_t + b \begin{bmatrix} \cos(\gamma + \alpha_0) \\ \sin(\gamma + \alpha_0) \end{bmatrix}, \quad (15)$$

to obtain

$$DE(\gamma) = \sqrt{|O_P O_G|_2^2 - (R_P - r_G)^2} \quad (16)$$

and the angles ψ_u and ψ_u^i as

$$\psi_u = \arccos\left(\frac{(O_P O_G)_x}{|O_P O_G|_2}\right), \quad \psi_u^i = \arcsin\left(\frac{DE}{|O_P O_G|_2}\right). \quad (17)$$

Finally, we compute the winding angle on the upper side of the mobile pulley as $\beta_u = \psi_u^i - \psi_u$. So, the total winding angle on the mobile lever pulley is $\beta_G = |\beta_l| + \beta_u$, on the motor pulley is $\beta_m = \pi - \theta - |\beta_l|$, and on the joint pulley is $\beta_P = q_1 + \frac{157.5}{180}\pi - \beta_u$. Now, we can formulate the congruence equation for the right branch of the transmission mechanism by expressing the length of the tendon as a function of the previously computed terms, obtaining

$$L_t = R_P \beta_m + BC + r_G \beta_G + DE + R_P \beta_P. \quad (18)$$

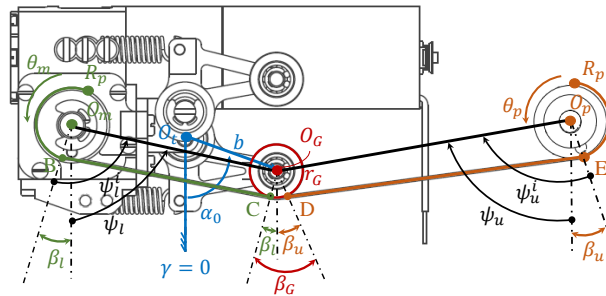


Figure 1. Schematic representation of the elastic transmission mechanism and definition of the geometric parameters required to derive the congruence equation.

Substituting $\delta = q_1 - \theta$ into (18) and solving the equation yield the desired function $\delta(\gamma)$. Next, we compute its derivative $\frac{\partial \delta}{\partial \gamma}$, we invert it, and substitute it into

$$\tau(\gamma) = -\frac{\partial U_s}{\partial \delta} = -\frac{\partial U_s}{\partial \gamma} \frac{\partial \gamma}{\partial \delta} = -\frac{\partial U_s}{\partial \gamma} \left(\frac{\partial \delta}{\partial \gamma} \right)^{-1} , \quad (19)$$

which is (20) from the main text, to obtain the torque delivered by the right branch of the elastic transmission on the motor shaft. The same procedure can be applied to the left branch of the actuation system. Given δ from the measurements of the encoders and assuming to know L_t by design, it is possible to solve (18) numerically to obtain γ , and thus the actuated torque. Finally, accounting for the contribution of the two branches yields the torque delivered to the actuated joint. Since the motor and joint pulleys have the same radii, to achieve the static equilibrium, the torque acting on the motor shaft τ_m must be of equal magnitude but opposite in verse to the one affecting the actuated joint τ_j , leading to

$$\tau_j = -\tau_m = \tau_r + \tau_l , \quad (20)$$

where τ_r and τ_l are the torques delivered by the right and left branches, respectively.